metals

MDPI

Article

Study on the Microstructure and Mechanical Properties of Non-Equimolar NiCoFeAlTi High Entropy Alloy Doped with Trace Elements

Chunfen Wu [1], Shuzhi Zhang [2,*], Jianchao Han [3], Changjiang Zhang [1] and Fantao Kong [4]

[1] School of Materials Science and Engineering, Taiyuan University of Technology, Taiyuan 030024, China
[2] School of Materials Science and Engineering, Yanshan University, Qinhuangdao 066004, China
[3] School of Mechanical and Vehicle Engineering, Taiyuan University of Technology, Taiyuan 030024, China
[4] College of Materials Science and Engineering, Harbin Institute of Technology, Harbin 150001, China
* Correspondence: shuzhizhang@outlook.com

Abstract: The method of improving the microstructure and thus the properties of alloys by adjusting their composition has been widely used in the study of high entropy alloys (HEAs). However, most studies have focused on improving the properties of HEAs with face-centered cubic (FCC) or body-centered cubic (BCC) structures by adjusting the contents of elements such as Ni, Al, Ti, Cr, Mn and Mo. The doping of B, Mg and Zr also has a certain effect on the mechanical properties of HEAs. In this paper, the phase structure, microstructure, and mechanical properties of $Ni_{45.5}Co_{22}Fe_{22}Al_5Ti_5$ HEA doped with B, Mg, and Zr were investigated. The results demonstrated that the three-phase structures of FCC matrix, $L1_2$ precipitate, and BCC phase were present in all the as-cast HEAs of $Ni_{45.5}Co_{22}Fe_{22}Al_5Ti_{5\times0.5}$ (X = B, Mg, and Zr). The microstructures of the as-cast alloys showed typical dendritic and inter-dendritic architecture. The maximum hardness was found in the alloy doped with B element, with a value of 433 HV. During the compressive test at room temperature, neither the Mg0.5 HEA nor the Zr0.5 HEA cracked until the load limit, but the B0.5 HEA cracked at a compressive strain of about 12%. B0.5 HEA had the highest compressive yield strength of the three alloys, followed by Zr0.5 HEA, while Mg0.5 HEA had the lowest, with values of 1030 MPa, 754 MPa, and 628 MPa, respectively. The work is expected to provide a boost for the research on the optimization of the properties of new HEAs reinforced by precipitation of $L1_2$ phase by providing a simple solution-microalloying method.

Keywords: high entropy alloys; B addition; Mg addition; Zr addition; phase structure; microstructure; mechanical property

check for updates

Citation: Wu, C.; Zhang, S.; Han, J.; Zhang, C.; Kong, F. Study on the Microstructure and Mechanical Properties of Non-Equimolar NiCoFeAlTi High Entropy Alloy Doped with Trace Elements. *Metals* **2023**, *13*, 646. https://doi.org/10.3390/met13040646

Academic Editor: Jiro Kitagawa

Received: 23 February 2023
Revised: 17 March 2023
Accepted: 22 March 2023
Published: 24 March 2023

Copyright: © 2023 by the authors. Licensee MDPI, Basel, Switzerland. This article is an open access article distributed under the terms and conditions of the Creative Commons Attribution (CC BY) license (https://creativecommons.org/licenses/by/4.0/).

1. Introduction

High entropy alloys (HEAs) are novel materials developed in recent years, which are generally composed of five or more principal elements, with the various elements having equal or near equal atomic percent (at. %) to each other. Due to their exceptional hardness, compressive strength, toughness, and thermal stability characteristics, HEAs have been widely studied. As a result of the generation of high entropy stable solid solution phases, multi-principal HEAs have excellent properties. Among them, FCC structure HEA is the most widely studied HEA system in recent years, which is composed of transition metal elements Cr, Co, Fe, Ni, Cu, etc. [1,2]. Many factors can influence the phase stability of HEAs, such as atomic size difference, electronegativity, mixing enthalpy, mixing entropy and valence electron concentration. When $\Delta H_{mix} < 0$, the binding force between alloying elements is strong, thus promoting the formation of intermetallic compounds. For alloys whose component atomic size differences are over 15%, it is most improbable to form a substitution solid solution. To obtain HEAs with good properties, it is necessary to select the correct combination of elements that have an impact on phase formation [3,4]. It should

also be noted that the mechanical properties of multi-principal HEAs are affected by the addition of alloying elements. The added alloying elements can interact with the alloy host elements to cause changes in the crystal structure of the alloy or the formation of ordered phases, which can affect the properties of the alloy. The addition of Al and Ti elements to promote the formation of $L1_2$ nano-precipitates in the alloy to strengthen the HEA has become the focus of researchers. However, the metastable $L1_2$ phase mainly strengthens the coherent interface FCC phase, and its stability is severely influenced by temperature. Other strengthening phases, such as $L2_1$ phase, hexagonal closed-packed (HCP) phase and even BCC phase, strongly enhance the strength, but dramatically reduce the ductility. Therefore, it is necessary to enhance the qualities of HEAs using particular strengthening procedures to achieve a balance between strength and ductility, such as grain boundary hardening, solid-solution hardening, precipitate hardening, and dislocation hardening [5–9].

It has been demonstrated that the mechanical properties of HEAs can be enhanced by microalloying. Boron (B) is an element with a small atomic radius. The addition of boron can effectively refine the grain size of both wrought-processed and cast alloys to obtain excellent mechanical properties [10]. Jae Bok Seol et al. introduced soluble boron into the FCC matrix and found that it led to an increase in the elastic-strain field of the internal grain structure of the alloy, resulting in the generation of cryogenic deformation-induced short-range order (SRO) domains at planar dislocation slip bands. As a result, $Fe_{40}Mn_{40}Co_{10}Cr_{10}$ and $Ni_{20}Fe_{20}Mn_{20}Co_{20}Cr_{20}$ (at. %) HEAs doped with soluble boron showed an increase in the cryogenic strength, especially a 32% increase in yield strength to 1.1 GPa [11]. An important effect of a very low concentration of boron (30 ppm) on the microstructure and mechanical properties of $(FeCoNiCr)_{88}Ti_6Al_6$ (at. %) HEA was reported by Yongliang Qi et al. Boron can eliminate the microcavity formed between the Heusler precipitates and matrix, suppress the formation and segregation of coarse Heusler precipitates, and promote the formation of $L1_2$ precipitates. These changes significantly improved the ductility and strength of $(FeCoNiCr)_{88}Ti_6Al_6$ HEA [12]. Yunus Azakli et al. studied the hardness of as-cast $Ni_{27}Al_{14}Cr$ alloy doped with Mg, and found that the microhardness of the alloy decreased when the magnesium content was low, and increased when the magnesium content was high. This was attributed to the formation of the Ni_3Al and Ni_2Mg phases, respectively. In the annealed state, the increase in hardness of the alloy was due to the solid solution formation of Mg in Ni_3Al and NiAl phases of the alloy [13]. Coarse or large-sized carbides damage the toughness and some high temperature properties of the alloy. The addition of Mg can promote the refinement of the grain boundary carbides. It was found that the addition of Mg to M17 Ni-based superalloy (no chemical formula, the main components of Ni, Co, Cr, Al, Ti and Mo, a small amount of V, Fe, C, Zr, Si and Mn) significantly changed the morphology of primary MC carbides (M represents the transition metal atoms and C represents the carbon atoms) in rapid directional solidification ingots from irregular surface to a smaller globular shape. The Mg enriched layer around the carbide may affect the transport of carbon and carbide forming elements across the interface and promote isotropic growth [14]. The diffusion of oxygen to the grain boundaries accelerates cavity nucleation and growth, making the alloy more susceptible to cracking. It has been reported that the addition of Zr and B counteracted the harmful effect of oxygen on interfacial energy, thereby preventing the early generation of microcracks and cavities on grain boundaries. This significantly improved the creep properties of nickel-based superalloys and increased the stress intensity threshold for creep crack growth [15,16]. It has also been shown that in IN100 Ni-based superalloy, the Zr element is more likely to stay at the interfacial boundaries between the eutectic pools and the matrix in the form of an intermetallic compound. The addition of Zr can reduce the solidus temperature of the alloy, affecting the solidification zone and promoting the formation of a low-melting point eutectic, which affects the properties of the alloy [17]. Mingxing Ma et al. reported that the addition of Zr to the equimolar ratio AlCoCrCuFe alloy significantly improved its hardness and wear resistance. This is due to the favorable influence of zirconium in refining the dendritic structure, improving the solid-solution

hardening efficiency and transforming the phase composition of the alloy from the FCC phase into high-strength HCP and BCC phases [18].

Based on the above discussion, $Ni_{45.5}Co_{22}Fe_{22}Al_5Ti_5X_{0.5}$ (X = B, Mg, Zr) HEAs were prepared in this study by adding the same content of B, Mg, and Zr trace elements. The microstructure and phase structure of $Ni_{45.5}Co_{22}Fe_{22}Al_5Ti_5X_{0.5}$ alloy were characterized to understand the effects of doping with different trace elements on the microstructure of the alloy. The relationship between the microstructure and mechanical properties of the alloy was investigated by hardness and room-temperature compression experiments. It is expected that the results can help identify the best doping element to improve the plasticity and strength of this alloy.

2. Materials and Methods

The HEA ingots with a nominal composition of $Ni_{45.5}Co_{22}Fe_{22}Al_5Ti_5X_{0.5}$ (at. %, X = B, Mg and Zr), denoted as B0.5, Mg0.5 and Zr0.5, respectively, were prepared by vacuum arc-melting the raw materials under an argon atmosphere. The purities of raw elemental materials were 99.9% for Ni, Co, Fe, Al, Ti and NiB (with Ni 82 at. % and B 18 at. %) and 99.5% for Zr and Mg. The HEA ingots with a weight of about 80 g were re-melted at least four times to improve chemical homogeneity.

The physical phase structure was identified by X-ray diffractometry (XRD, SmartLsb SE) using Cu Kα radiation at a scanning rate of 6° min^{-1} and a 2θ range of 20–100°. Scanning electron microscopy (SEM, ZEISS Gemini 300, Carl Zeiss AG, Jena, Germany) and field emission electron microscopy (TEM, FEI Tecnai 30, Philips-FEI, Amsterdam, the Netherlands) were used to characterize microstructures. Electron backscatter diffraction (EBSD) analysis was performed by using scanning electron microscopy (SEM, JEOL-JSM-IT500, JEOL, Tokyo, Japan) equipped with channel5 software (HKL Channel 5.0, Oxford Instrument, Oxford, UK).

The samples for SEM examination were first polished to 2000-grit with SiC paper before being electrochemically polished with a polishing solution containing 10% $HClO_4$ and 90% C_2H_5OH at a direct voltage of 25 V. The hardness of the samples was measured by using a micro-Vickers hardness tester (HVT-1000, Lunjie Electromechanical Instrument, Shanghai, China) with a load of 500 g for a duration of 15 s. The average hardness value for each alloy was calculated by measuring it at five different locations. The room temperature compressive mechanical properties were tested on an electronic universal material testing machine (INSTRON 5969, Instron Corporation, Boston, MA, USA) at a loading rate of 1.0×10^{-3} s^{-1}, and a load of no more than 45 kN. For the room temperature compressive test, a cylindrical sample of Φ4 mm × 6 mm was cut from the ingot. To reduce experimental error, three compression tests were performed for each alloy to obtain the average value.

3. Results and Discussion

3.1. Microstructure

The XRD patterns of the three as-cast HEAs of B0.5, Mg0.5, and Zr0.5 are shown in Figure 1a. The diffraction peaks for face-centered cubic (FCC) structure and body-centered cubic (BCC) structure are observed in all alloys. The intensity of the FCC diffraction peaks in the three HEAs is higher than that of the BCC diffraction peaks, indicating that the content of FCC phase in the three HEAs is higher than that of the BCC phase. Combined with the microstructure shown in Figure 2, the FCC diffraction peaks overlap with those of the $L1_2$ phase, so the diffraction peaks of the $L1_2$ phase cannot be distinguished in the XRD pattern. This may be due to the small particle size of $L1_2$ precipitates and the peak broadening effect caused by the similar crystal structure of these precipitates and the matrix. At the same time, some studies have shown that there is a coherent interface between the matrix FCC and the $L1_2$ phase, which also makes it more difficult to distinguish the diffraction peaks of the $L1_2$ phase [19,20]. Since the elements Mg and Zr have much larger atomic radius than the element B, the dissolution of Mg or Zr into the alloy causes the FCC peaks of Mg0.5 and Zr0.5HEA to shift slightly to the left, as shown in Figure 1b.

Due to the small doping amount, the peak deviation amplitude is not considerable. The results show that the lattice parameters of the FCC phase in Mg0.5 and Zr0.5 alloys are larger than those of the B0.5 alloy [21,22]. The lattice parameters of the three HEAs were obtained from the corresponding refined XRD patterns. The lattice constants (a) of the FCC phase in B0.5, Mg0.5 and Zr0.5 alloys were calculated to be 3.5937, 3.6051 and 3.6036 Å, respectively. The three as-cast HEAs have nearly the same lattice parameter. The lattice constants of Mg0.5 and Zr0.5 are slightly larger than that of B0.5.

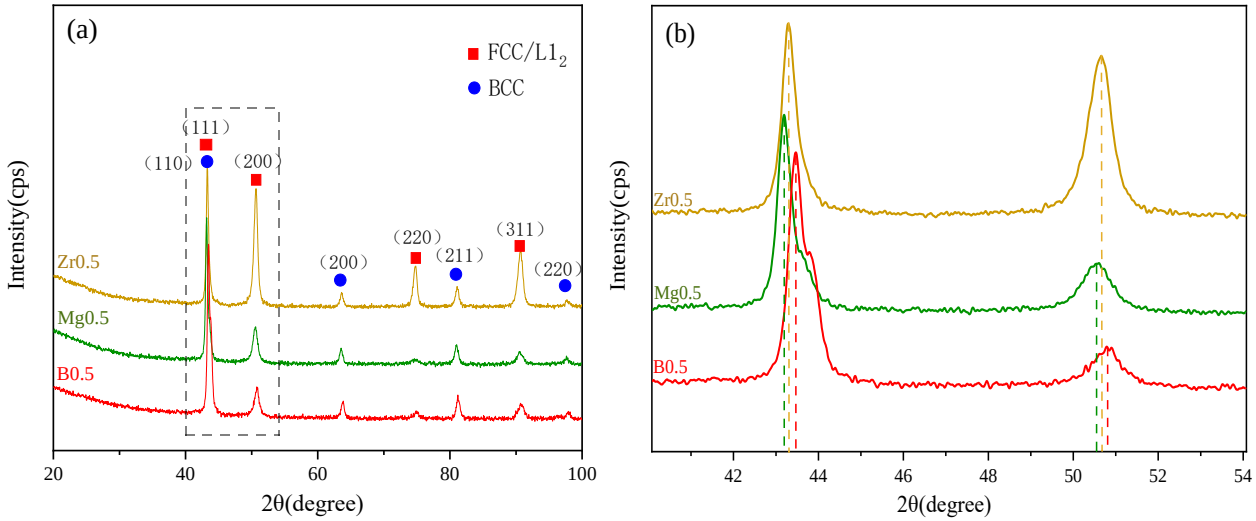

Figure 1. (**a**) X-ray diffraction patterns of the three HEA samples (B0.5, Mg0.5, and Zr0.5) in the as-cast state; (**b**) an enlarged view of the peaks (111) and (200) at 40° to 55° in (**a**).

Figure 2 shows the SEM micrographs of the as-cast alloys. All the alloys exhibit typical casting dendritic and inter-dendrite morphology. Due to the high cooling speed of the vacuum arc-melting technique, constitutional supercooling of the cast ingot increases to make a dendrite structure. According to literature reports, the microstructure of some other types of alloys also showed a typical dendrite morphology. For example, Zr was added to the AlCoCrCuFe HEA with equal molar ratio and the dendrite structure was refined significantly [18]. Moreover, $Ni_{40}Fe_{30}Co_{20}Al_{10}$ and $(Ni_{40}Fe_{30}Co_{20}Al_{10})_{90}Ti_{10}$ HEAs both exhibited trench-like interdendrite and cellular-like dendrite structures. It was found that the dendrite structure of the alloy was finer after the addition of Ti [23]. Compared with the microstructure of the Zr0.5 alloy and the Mg0.5 alloy, the B0.5 alloy has well-developed primary dendrite arms and poorly-developed secondary dendrite arms, with long primary dendrite arms. This result demonstrates that the B element has weaker constitutional supercooling effects compared to the Mg element and Zr element on this HEA. In the high magnification image of the inter-dendrite region (Figure 2b), a black region and numerous nano precipitates are observed. The black region is the enlarged morphology of the strip-like bulge in the inter-dendrite region in Figure 2a. Combined with XRD and SEM analyses of the alloy, it can be preliminarily inferred that the nano precipitate is the $L1_2$ phase in the FCC matrix, and the black region is the BCC phase. Furthermore, the FCC/$L1_2$ mixed structure can be observed in the BCC phase, as shown in Figure 2b. At the junction of the FCC matrix and the BCC phase, there are a few coarsened $L1_2$ phases. Unlike the finely spherical nanoparticles that are uniformly distributed far from the boundaries of the black region, these particles appear as elongated strips. This may be due to the non-uniform distribution of elements in the as-cast alloy, which causes the segregation of some elements near the phase boundaries [23–25]. The dendritic and inter-dendritic microstructure of the as-cast Mg0.5 alloy (Figure 2c) is coarser than that of B0.5 HEA and Zr0.5 HEA. Numerous approximately spherical $L1_2$ precipitates are uniformly scattered, as seen in Figure 2d. However, other precipitated phases with different morphologies are not

observed in Figure 2d. Further research must be conducted to pinpoint the exact position of the BCC phase. The histomorphology of the as-cast Zr0.5 alloy (Figure 2e,f) is similar to that of the as-cast B0.5 alloy. The Zr0.5 alloy also has a BCC phase and FCC/$L1_2$ mixed structure. For further quantitative analysis of precipitated phase, the statistics of the size of $L1_2$ precipitates in the as-prepared alloys are obtained by image-pro plus software. For the convenience of statistics and analysis, $L1_2$ precipitates are regarded as spheres. The average particle sizes of $L1_2$ precipitates inside the grains of the three alloys are 41.45 nm (B0.5), 58.76 nm (Mg0.5) and 49.90 nm (Zr0.5). It is seen that the average particle size of $L1_2$ particles in the alloy doped with B is relatively small, followed by the Zr0.5 and Mg0.5 alloys. Compared to Mg and Zr, the addition of B contributes more to the size refinement of the $L1_2$ precipitates in the alloy.

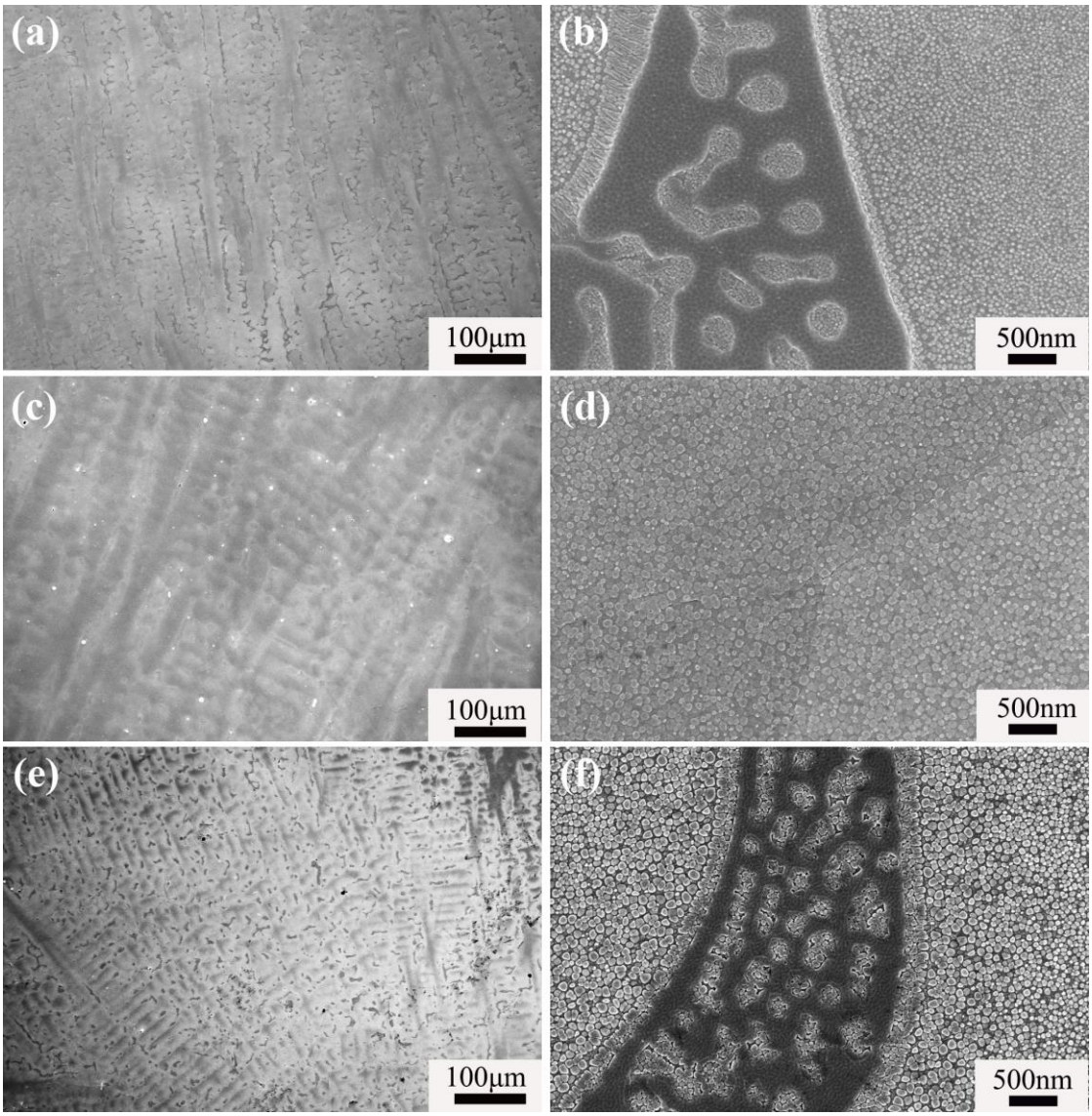

Figure 2. Secondary electron (SE) images of the three HEAs in the as-cast state. (**a**,**b**) B0.5 HEA; (**c**,**d**) Mg0.5 HEA; (**e**,**f**) Zr0.5 HEA. All alloys are shown at both low and high magnifications.

As illustrated in Figure 3, the precise positions of the FCC and BCC phases were investigated using the EBSD technique. The FCC and BCC phases are represented by yellow and red hues, respectively. As seen in Figure 3b, the BCC phase is mainly distributed in the inter-dendritic region of the B0.5 HEA, and a small number of FCC phases are also observed in the BCC phase. As seen in Figure 3d, BCC phase is mainly observed in the

grain boundary region of the Mg0.5 alloy, and its proportion in the phase diagram is 0.4%. The proportion of BCC phase in the Zr0.5 alloy is about 0.8%, which shows a short rod-like morphology. The relative proportion of BCC phase in the B0.5 alloy is the highest, about 13%. Compared with Mg and Zr, the addition of B promotes the formation of BCC phase in the alloy. Combined with SEM analysis, it is evident that the addition of Mg has no significant effect on the size of $L1_2$ particles at the phase boundary, while the addition of B significantly increases the size of $L1_2$ particles near the BCC phase distributed along the grain boundary. The inhomogeneous distribution of elements in the as-cast alloy may be the cause of this phenomenon. It may also be caused by the segregation of Ti elements at the grain boundaries [22,26].

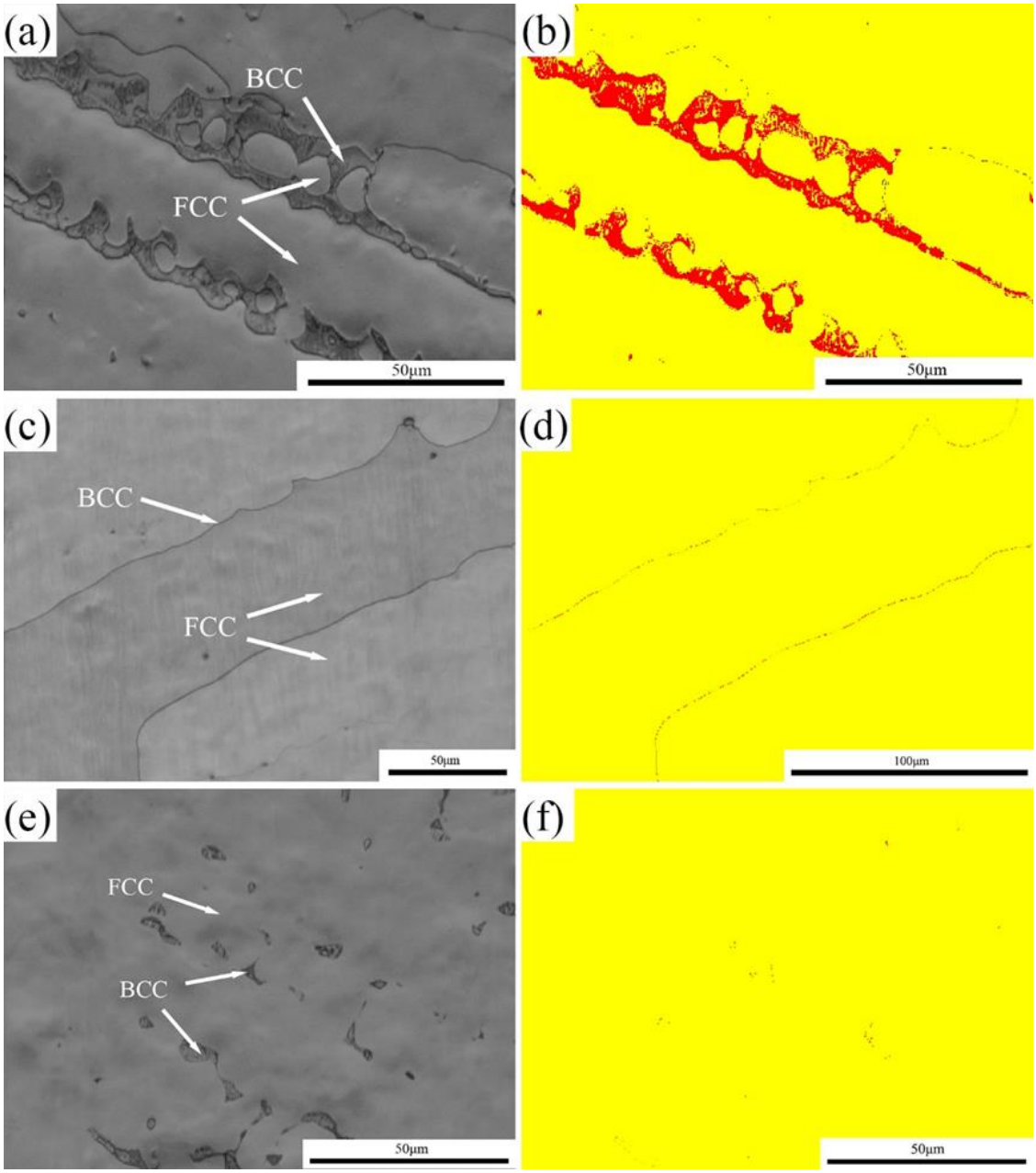

Figure 3. EBSD BC and phase images of the as-cast alloy samples. (**a**,**c**,**e**) are BC images for B0.5, Mg0.5, and Zr0.5 HEAs, respectively; (**b**,**d**,**f**) are the phase images of B0.5, Mg0.5, and Zr0.5 HEAs, respectively.

A TEM investigation was conducted to reveal the complex microstructure of the as-cast B0.5 HEA, as illustrated in Figure 4. The bright-field image of the as-cast B0.5 HEA is depicted in Figure 4a, which shows the BCC phases and the FCC matrices, which are denoted by yellow and red dashed circles, respectively. Notably, several fine precipitates can be found in the FCC matrix. Two diffraction spots are observed in the selected area electron diffraction (SAED) patterns (Figure 4b,c), corresponding to the different color regions. This confirms that the matrix and precipitate have FCC and BCC crystal structures, respectively. The FCC matrix and $L1_2$ precipitate particles (Figure 4c) are both confirmed by the [0 −1 1] FCC SAED pattern [21,22]. The high-resolution transmission electron microscopy (HRTEM) image (Figure 4d) and the corresponding fast Fourier transformation (FFT) image (Figure 4e,f) further demonstrate that the matrix and fine precipitates have a disordered FCC crystal structure and an ordered $L1_2$ superlattice structure, respectively.

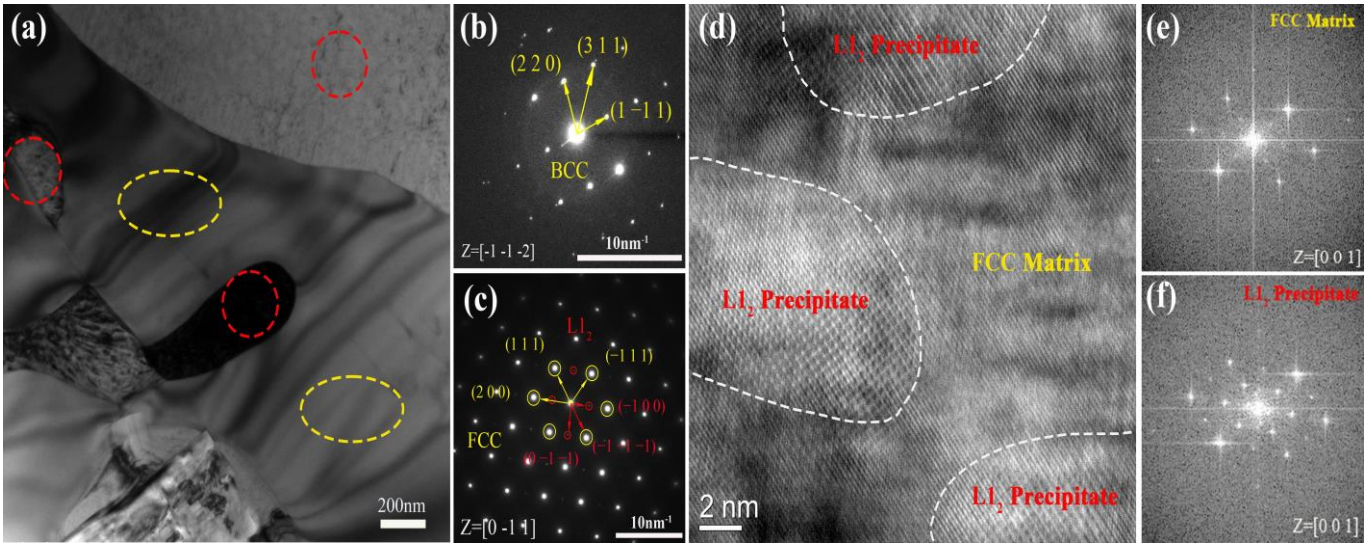

Figure 4. TEM images of the as-cast B0.5 HEA showing the complex microstructure morphology. (**a**) is the bright-field (BF) image of B0.5 HEA; (**b**,**c**) are the selected area electron diffraction (SAED) patterns of BCC and FCC phases, respectively. (**d**) is the high-resolution TEM (HRTEM) of the FCC matrix and $L1_2$ precipitate interface; (**e**,**f**) are the fast Fourier transform (FFT) images of the FCC matrix and $L1_2$ precipitate, respectively.

HAADF-STEM images and STEM-EDX maps of the three as-cast HEAs are shown in Figure 5. According to the preceding discussion, the different regions in the B0.5 HEA (Figure 5a) are denoted by points A, B, and C, respectively. The specific elemental content of each point is shown in Table 1. It can be observed that point A is enriched in Ni, Co, and Ti elements but depleted in Al. Point A is the BCC precipitate, as confirmed by the [−1 −1 −2] SAED pattern in Figure 4b, with an average chemical composition of Ni: 48.7 at. %, Co: 28.0 at. %, Fe: 13.7 at. %, Al: 0.2 at. %, and Ti: 9.4 at. %. The [0 −1 1] SAED pattern in Figure 4c confirms the existence of both the FCC matrix and the $L1_2$ precipitates at point B. The average chemical composition at this point is Ni: 45.9 at. %, Co: 23.7 at. %, Fe: 26.0 at. %, Al: 1.8 at. %, and Ti: 2.6 at. %. Point C is enriched with Ti and B elements. Formation of intermetallic compounds is promoted by the relatively high negative mixing enthalpy between Ti and B elements. It has been demonstrated that Ti addition has little effect on the dendritic morphology of as-cast Ni-rich HEAs, but causes severe component segregation in the matrix, which further promotes the formation of the BCC phase. Therefore, it is speculated that a rod-like boride with a Ti-rich phase may be mainly distributed near the BCC phase [21,26–28]. From the STEM-EDX images of the Mg0.5 HEA in Figure 5b, it can be seen that the matrix contains a large number of spherical-like precipitates that are uniformly distributed. The precipitates are mainly rich in Ni, Al, and Ti elements and poor in Co and Fe elements. The distribution of elements in the matrix has the opposite trend of

these precipitates. This phenomenon can also be seen in the STEM-EDX images of the Zr0.5 HEA in Figure 5c. Specifically, the $L1_2$ precipitate is enriched in Ni, Al, and Ti elements, but depleted in Co and Fe elements. In contrast, the FCC phase is enriched in Fe and Co elements and poor in Ni, Al, and Ti elements. The above results verify that the matrix and precipitates in the three as-cast HEAs are indeed FCC phase and $L1_2$ precipitates, respectively. The stoichiometry of $L1_2$ precipitates may be (Ni, Co, Ti)$_3$(Al, Ti) [22–24]. From the STEM-EDX images of the Mg0.5 HEA in Figure 5b-6, it can be seen that the Mg element is uniformly distributed throughout the matrix. However, no significant changes in elemental composition are found near the grain boundaries, which is the possible BCC phase distribution. The STEM-EDX mapping results of the Zr0.5 HEA are shown in Figure 5c. Ni is more uniformly distributed, Al is mainly distributed in the FCC/$L1_2$ mixed structure, while Zr prefers to exist in the BCC phase. Co and Fe elements are enriched in the FCC matrix, and Ti is enriched in $L1_2$ nano precipitates. Moreover, although Ni is distributed relatively uniformly, it is enriched in $L1_2$ nano precipitates [21,27–29]. Due to the relatively low content of added trace elements, the specific contents of B and Mg elements detected (Table 1) are also extremely low. Even though the presence of these trace elements is not detected, the differences in their microstructure suggest that the trace elements are crucial to the distribution of other elements in the dendrites and inter-dendrites as well as the final microstructure.

Table 1. Chemical composition of the three as-cast HEAs obtained by TEM-EDS (at. %).

Regions	Compositions					
	Ni	**Co**	**Fe**	**Al**	**Ti**	**B/Mg/Zr**
B0.5 (A)	48.7	28.0	13.7	0.2	9.4	0
B0.5 (B)	45.9	23.7	26.0	1.8	2.6	0
B0.5 (C)	8.6	6.6	7.5	0.2	69.4	7.7
B0.5	49.3	21.0	20.9	2.8	5.5	0.5
Mg0.5	47.0	21.9	22.2	2.8	5.2	0.9
Zr0.5	50.3	19.5	13.6	2.2	7.3	7.1

3.2. Room-Temperature Hardness

Figure 6 displays the average micro-Vickers hardness values and standard deviations for the three as-cast HEAs, as measured by the Vickers hardness tester at room temperature. It can be seen that the B0.5 HEA has the highest hardness (433 HV), followed by the Zr0.5 HEA (380 HV) and the Mg0.5 HEA (365 HV). The corresponding standard deviations are 14.42 HV, 5.98 HV and 3.01 HV, respectively. The results show that the hardness of Mg0.5 and Zr0.5 HEAs is lower than that of B0.5 HEA. The hardness of the alloy is affected not only by the type of phase in the microstructure but also by its content. All the HEAs have FCC/$L1_2$ phase and BCC phase, according to XRD and EBSD analyses. Compared with B0.5 alloy, the FCC phase fraction is more dominant in Mg0.5 and Zr0.5 HEAs. It is worth noting that FCC has more slip directions and is more susceptible to slip deformation than BCC. This may result in a more plastic but less hard alloy for FCC structures. Although Mg and Zr with large atomic radius have better solution strengthening effect than B, this effect may be weaker than the phase weakening of large volume fraction FCC crystal structure. As a result, Mg0.5 and Zr0.5 alloys have a lower hardness value than the B0.5 alloy. Although the proportion of the FCC phase in the Mg0.5 HEA is approximately the same as the Zr0.5 HEA, the hardness of the Zr0.5 alloy is higher than that of the Mg0.5 alloy. This may be because the addition of the Zr element can greatly refine the microstructure of the alloy. In addition, Zr has a larger atomic radius than Mg, which increases the distortion of the cell and enhances solid solution hardening. Hence, it not only reduces the grain size of the alloy but also increases the number of dislocations in the alloy, which increases the brittle tendency of the alloy and leads to slightly higher hardness than Mg0.5 HEA [18,30–32].

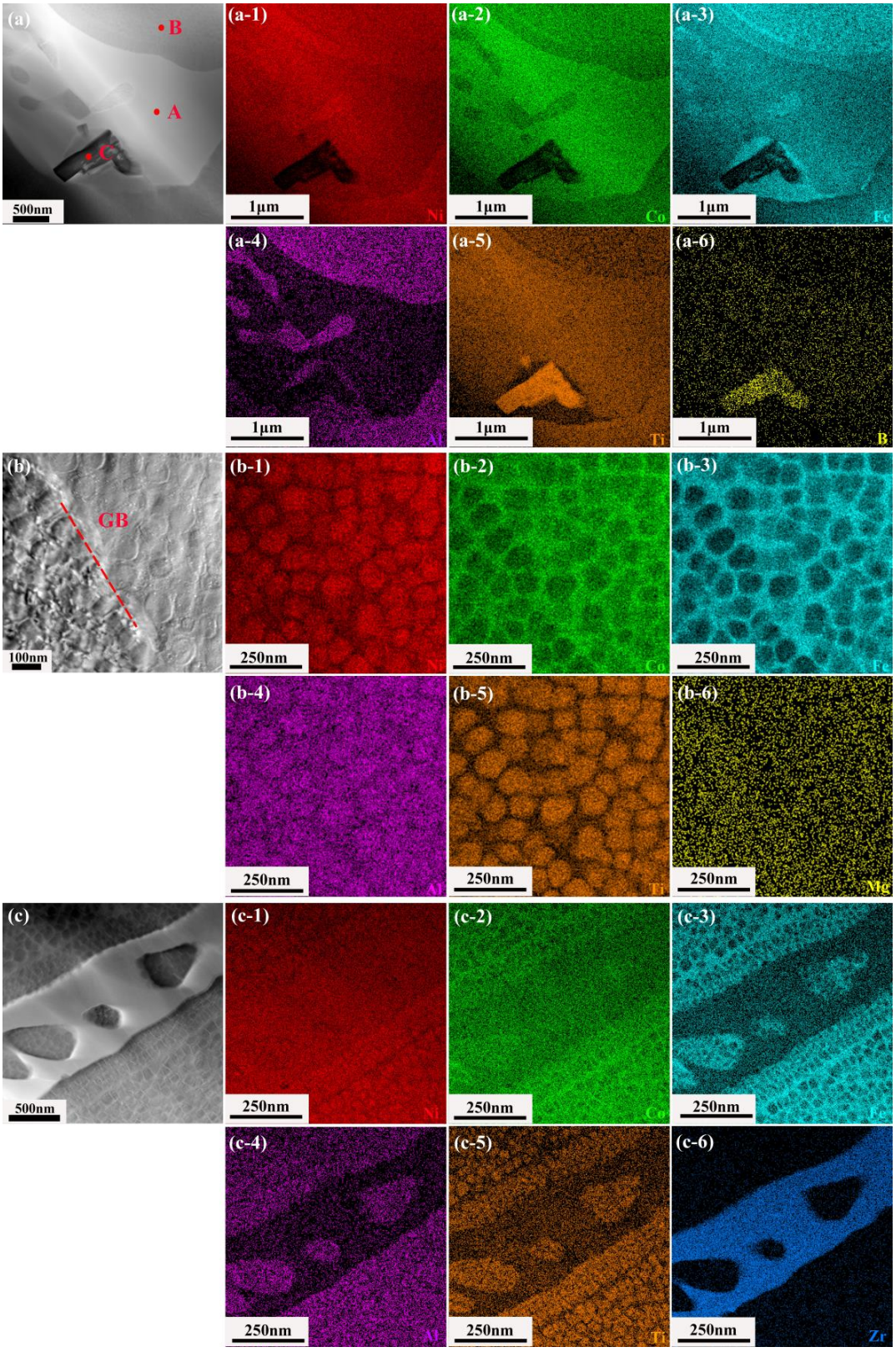

Figure 5. HAADF-STEM image and corresponding STEM-EDX elemental maps of the three as-cast HEAs. (**a**) B0.5 HEA, (**a-1**–**a-6**) EDS compositional distribution mapping of the Ni, Co, Fe, Al, Ti, and B elements; (**b**) Mg0.5 HEA, (**b-1**–**b-6**) EDS compositional distribution mapping of the Ni, Co, Fe, Al, Ti, and Mg elements; (**c**) Zr0.5 HEA, (**c-1**–**c-6**) EDS compositional distribution mapping of the Ni, Co, Fe, Al, Ti, and Zr elements.

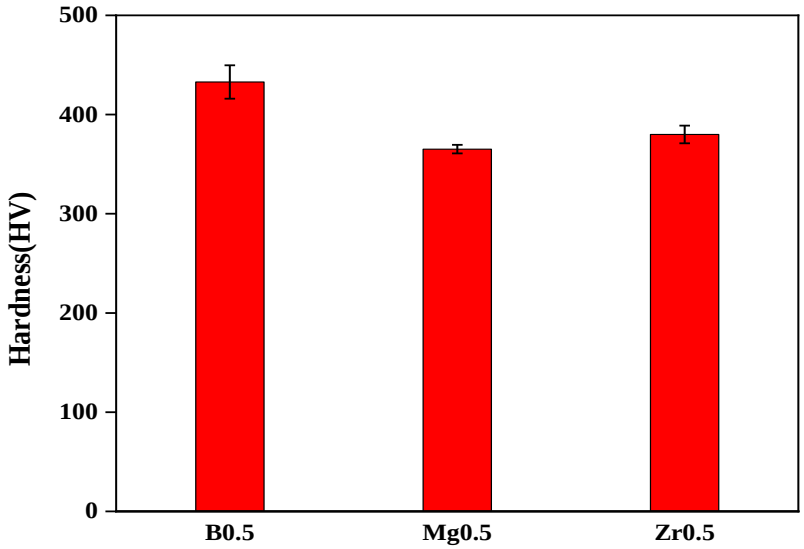

Figure 6. Average hardness values and deviations of the B0.5, Mg0.5, and Zr0.5 HEAs.

3.3. Compressive Properties

Figure 7 presents the room-temperature compressive stress-strain curves of the HEAs doped with various trace elements at a strain rate of 1.0×10^{-3} s^{-1}. The compressive mechanical properties of the HEAs were tested at loads up to 45 kN due to the restrictions of the experimental conditions. As shown in Figure 7, the B0.5 HEA cracks at a compressive strain of about 12%, while neither the Mg0.5 HEA nor the Zr0.5 HEA fractures at room temperature until the load limit. When the load limit is reached, the compressive deformation quantity is close to 30%. This suggests that the plasticity of the Mg0.5 and Zr0.5 HEAs is greater than that of the B0.5 HEA. Comparing the compressive yield strengths of the HEAs, the B0.5 HEA has the highest yield strength, followed by the Zr0.5 and Mg0.5 HEAs, with the values of 1030 MPa, 754 MPa, and 628 MPa, respectively. The standard deviations of the yield strength results of the alloys are 29 MPa, 22 MPa and 87 MPa, respectively. It is seen that the yield strength values of these HEAs follow the same trend as the Vickers hardness (HV) values. The B0.5 HEA has the lowest compressive strength of 1830 MPa and a compressive strain of 12%. The standard deviations of compressive strain and compressive strength results are 251 MPa and 2%.

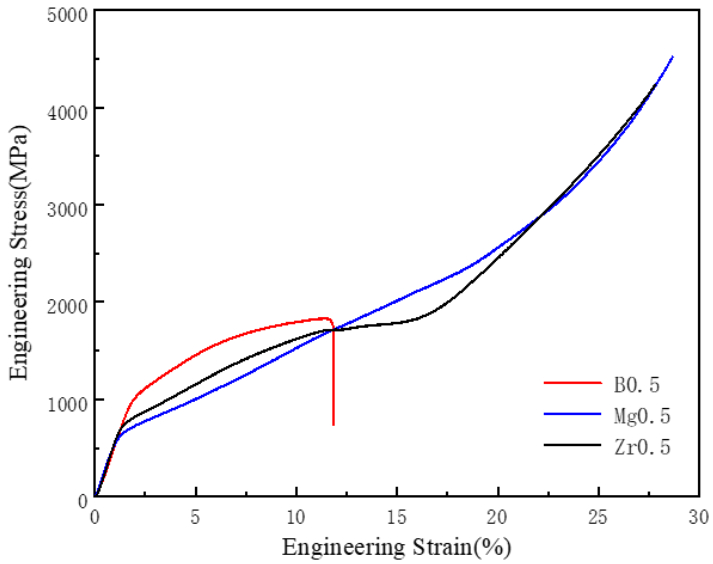

Figure 7. Compressive stress-strain curves of the B0.5, Mg0.5, and Zr0.5 HEAs.

The average values of the elastic modulus of each alloy obtained by room temperature compression experiment are 57.31 GPa (B0.5), 42.40 GPa (Mg0.5), and 53.10 GPa (Zr0.5), respectively. The results show that the alloys with B have higher elastic modulus than those with Mg or Zr. Compared with B doped alloy, the addition of Zr or Mg reduces the elastic modulus of the alloy, thus reducing the stiffness of the material.

As illustrated in Figures 2 and 3, the highest fraction of the BCC phase in B0.5 HEA is the main factor responsible for its low compressive strain and the high compressive yield strength. In contrast, the Mg0.5 and Zr0.5 HEAs have better plasticity because the FCC/$L1_2$ structure has more slip systems and the grains are better able to coordinate deformation during the plastic deformation. Solid solution strengthening and precipitation strengthening are the main strengthening mechanisms of the alloys. The integration of solute atoms with different atomic sizes into the solid solution causes lattice distortion. Since the atomic sizes of the added Mg and Zr are much larger, the lattice distortion energy increases significantly and the solid solution strengthening is enhanced after the atoms enter the crystalline lattice, which also plays a certain role in improving the strength of the alloy. Combined with the microstructure analysis of the alloy, it is evident that the size and volume fraction of the precipitate particles of the alloy doped with different trace elements are different. The $L1_2$ precipitates have a co-lattice relationship with the FCC matrix. The increase in the particle size and volume fraction of $L1_2$ precipitates enhances the hindrance effect on the dislocation movement, which leads to an increase in the strength of the alloy. Since the BCC precipitates and the FCC matrix belong to the non-lattice relationship, the mismatch is large, which promotes the crack initiation of the B-doped alloy, resulting in a rapid decrease in plasticity. Therefore, the strength of HEAs can be effectively increased by adding trace elements to enhance the second phase strengthening [12,33–35].

4. Conclusions

In this work, HEA ingots with nominal compositions of $Ni_{45.5}Co_{22}Fe_{22}Al_5Ti_5B_{0.5}$, $Ni_{45.5}Co_{22}Fe_{22}Al_5Ti_5Mg_{0.5}$, and $Ni_{45.5}Co_{22}Fe_{22}Al_5Ti_5Zr_{0.5}$ were fabricated by vacuum arc melting. XRD, SEM, EBSD, and TEM characterizations were used to analyze the changes in the microstructures and mechanical properties of the HEAs doped with various trace elements at room temperature. From this work, the following conclusions can be made.

(1) All the as-cast alloys display typical dendritic and inter-dendritic morphology. B element has weaker constitutional supercooling effects than Mg and Zr elements, which results in well-developed primary dendrite arms and poorly-developed secondary dendrite arms in the B0.5 alloy.

(2) All three alloys are composed of BCC phase, FCC phase, and $L1_2$ nano phase precipitated in FCC phase. In comparison to Mg and Zr elements, the average particle size of $L1_2$ precipitates in the alloy doped with B is relatively small. To a certain extent, the addition of B can promote the formation of $L1_2$ nano-precipitates with smaller particle sizes in the alloy.

(3) Due to the high content of BCC in the B0.5 alloy, it has the highest hardness and compression yield strength. FCC is more susceptible to slip deformation than BCC, resulting in more plasticity but lower hardness in Mg0.5 and Zr0.5 alloys with predominant FCC structure. The B0.5 alloy has the lowest compressive strain. The Zr0.5 alloy has a higher hardness than the Mg0.5 alloy, due to the solution strengthening and microstructure refining effects of the Zr element. Solid solution strengthening and precipitates strengthening are the main strengthening mechanisms of these alloys.

Author Contributions: Conceptualization, C.Z.; methodology, J.H. and F.K.; writing—original draft preparation, C.W.; writing—review and editing, S.Z. All authors have read and agreed to the published version of the manuscript.

Funding: This research was funded by the National Natural Science Foundation of China (52071228, 52171122, 52275362), the Key Research and Development program of Shanxi Province (No. 201903D121056), and the APC was funded by Harbin Institute of Technology.

Data Availability Statement: Data are contained within the article.

Conflicts of Interest: The authors declare no conflict of interest.

References

1. Zhang, Y.; Zuo, T.T.; Tang, Z.; Gao, M.C.; Dahmen, K.A.; Liaw, P.K.; Lu, Z.P. Microstructures and properties of high-entropy alloys. *Prog. Mater. Sci.* **2014**, *61*, 1–93. [CrossRef]
2. Miracle, D.B.; Senkov, O.N. A critical review of high entropy alloys and related concepts. *Acta Mater.* **2017**, *122*, 448–511. [CrossRef]
3. Mandal, P.; Choudhury, A.; Mallick, A.B.; Ghosh, M. Phase Prediction in High Entropy Alloys by Various Machine Learning Modules Using Thermodynamic and Configurational Parameters. *Met. Mater. Int.* **2022**, *29*, 38–52. [CrossRef]
4. Zhang, Y.; Zhou, Y.J.; Lin, J.P.; Chen, G.L.; Liaw, P.K. Solid-Solution Phase Formation Rules for Multi-component Alloys. *Adv. Eng. Mater.* **2008**, *10*, 534–538. [CrossRef]
5. Gangireddy, S.; Gwalani, B.; Soni, V.; Banerjee, R.; Mishra, R.S. Contrasting mechanical behavior in precipitation hardenable AlXCoCrFeNi high entropy alloy microstructures: Single phase FCC vs. dual phase FCC-BCC. *Mater. Sci. Eng. A* **2019**, *739*, 158–166. [CrossRef]
6. Liu, M.; Li, W.; Lin, S.; Fu, H.; Li, H.; Wang, A.; Lin, X.; Zhang, H.; Zhu, Z. Dislocation slip induced tensile plasticity and improved work-hardening capability of high-entropy metallic glass composite. *Intermetallics* **2022**, *141*, 107407. [CrossRef]
7. Qi, Y.L.; Zhao, L.; Sun, X.; Zong, H.X.; Ding, X.D.; Jiang, F.; Zhang, H.L.; Wu, Y.K.; He, L.; Liu, F.; et al. Enhanced mechanical performance of grain boundary precipitation-hardened high-entropy alloys via a phase transformation at grain boundaries. *J. Mater. Sci. Technol.* **2021**, *86*, 271–284. [CrossRef]
8. Traversier, M.; Mestre-Rinn, P.; Peillon, N.; Rigal, E.; Boulnat, X.; Tancret, F.; Dhers, J.; Fraczkiewicz, A. Nitrogen-induced hardening in an austenitic CrFeMnNi high-entropy alloy (HEA). *Mater. Sci. Eng. A* **2021**, *804*, 140725. [CrossRef]
9. He, J.Y.; Wang, H.; Huang, H.L.; Xu, X.D.; Chen, M.W.; Wu, Y.; Liu, X.J.; Nieh, T.G.; An, K.; Lu, Z.P. A precipitation-hardened high-entropy alloy with outstanding tensile properties. *Acta Mater.* **2016**, *102*, 187–196. [CrossRef]
10. Yamaguchi, M.; Inui, H.; Ito, K. High-temperature structural intermetallics. *Acta Mater.* **2000**, *48*, 307–322. [CrossRef]
11. Seol, J.B.; Bae, J.W.; Kim, J.G.; Sung, H.; Li, Z.; Lee, H.H.; Shim, S.H.; Jang, J.H.; Ko, W.-S.; Hong, S.I.; et al. Short-range order strengthening in boron-doped high-entropy alloys for cryogenic applications. *Acta Mater.* **2020**, *194*, 366–377. [CrossRef]
12. Qi, Y.; Cao, T.; Zong, H.; Wu, Y.; He, L.; Ding, X.; Jiang, F.; Jin, S.; Sha, G.; Sun, J. Enhancement of strength-ductility balance of heavy Ti and Al alloyed FeCoNiCr high-entropy alloys via boron doping. *J. Mater. Sci. Technol.* **2021**, *75*, 154–163. [CrossRef]
13. Azakli, Y.; Tarakci, M. Towards understanding the effects of magnesium addition on microstructural and thermal properties of NiAlCr alloys in as-cast and heat treated states. *J. Alloys Compd.* **2017**, *699*, 151–159. [CrossRef]
14. Ge, H.L.; Youdelis, W.V.; Chen, G.L.; Zhu, Q. Interfacial segregation of magnesium in nickel base superalloy: Carbide morphology and properties. *Mater. Sci. Technol.* **2013**, *5*, 985–990. [CrossRef]
15. Floreen, S.; Davidson, J.M. The effects of b and zr on the creep and fatigue crack growth behavior of a Ni-base superalloy. *Met. Trans. A* **1983**, *14*, 895–901. [CrossRef]
16. Kalavathi, V.; Kumar Bhuyan, R. A detailed study on zirconium and its applications in manufacturing process with combinations of other metals, oxides and alloys—A review. *Mater. Today Proc.* **2019**, *19*, 781–786. [CrossRef]
17. Zhou, Y.; Wang, B.; Li, S.; Li, W.; Xu, K.; Liang, J.; Zhou, F.; Wang, C.; Wang, J. On the segregation behavior and influences of minor alloying element Zr in nickel-based superalloys. *J. Alloys Compd.* **2022**, *897*, 163169. [CrossRef]
18. Ma, M.; Wang, Z.; Zhou, J.; Song, M.; Zhang, D.; Zhu, D. Effect of Zr Additions on Phase Transformations, Microstructure and Wear Resistance of High-Entropy AlCoCrCuFe Alloy. *Met. Sci. Heat Treat.* **2022**, *63*, 470–478. [CrossRef]
19. Zhao, Y.L.; Yang, T.; Tong, Y.; Wang, J.; Luan, J.H.; Jiao, Z.B.; Chen, D.; Yang, Y.; Hu, A.; Liu, C.T.; et al. Heterogeneous precipitation behavior and stacking-fault-mediated deformation in a CoCrNi-based medium-entropy alloy. *Acta Mater.* **2017**, *138*, 72–82. [CrossRef]
20. Zheng, T.; Hu, X.; He, F.; Wu, Q.; Han, B.; Chen, D.; Li, J.; Wang, Z.; Wang, J.; Kai, J.-j.; et al. Tailoring nanoprecipitates for ultra-strong high-entropy alloys via machine learning and prestrain aging. *J. Mater. Sci. Technol.* **2021**, *69*, 156–167. [CrossRef]
21. Seol, J.B.; Bae, J.W.; Li, Z.; Chan Han, J.; Kim, J.G.; Raabe, D.; Kim, H.S. Boron doped ultrastrong and ductile high-entropy alloys. *Acta Mater.* **2018**, *151*, 366–376. [CrossRef]
22. Chen, J.; Niu, P.; Liu, Y.; Lu, Y.; Wang, X.; Peng, Y.; Liu, J. Effect of Zr content on microstructure and mechanical properties of AlCoCrFeNi high entropy alloy. *Mater. Des.* **2016**, *94*, 39–44. [CrossRef]
23. Niu, Z.; Xie, Y.; Axinte, E.; Xu, J.; Wang, Y. Development and characterization of novel Ni-rich high-entropy alloys. *J. Alloys Compd.* **2020**, *846*, 156342. [CrossRef]
24. Xu, H.; Li, Z.; Zhou, W.; Ma, L.; Zhang, M.; Li, G. Aluminum and titanium alloyed non-equiatomic Co–Fe–Ni medium-entropy alloy with ultra high strength and hardness. *Mater. Sci. Eng. A* **2021**, *817*, 141297. [CrossRef]
25. Jia, Z.Y.; Zhang, S.Z.; Zheng, L.W.; Zhang, W.G.; Zhang, C.J.; Kong, F.T. Multi-principal element intermetallic based alloy with excellent mechanical properties by thermo-mechanical treatment. *Mater. Lett.* **2022**, *314*, 131861. [CrossRef]

26. Jia, Z.Y.; Zhang, S.Z.; Huo, J.T.; Zhang, C.J.; Zheng, L.W.; Kong, F.T.; Li, H. Heterogeneous precipitation strengthened non-equiatomic NiCoFeAlTi medium entropy alloy with excellent mechanical properties. *Mater. Sci. Eng. A* **2022**, *834*, 142617. [CrossRef]
27. Huang, X.; Huang, L.; Peng, H.; Liu, Y.; Liu, B.; Li, S. Enhancing strength-ductility synergy in a casting non-equiatomic NiCoCr-based high-entropy alloy by Al and Ti combination addition. *Scr. Mater.* **2021**, *200*, 113898. [CrossRef]
28. Liu, L.; Zhang, Y.; Wu, G.; Yu, Y.; Ma, Y.; Ma, J.; Baker, I.; Zhang, Z. The effect of Al/Ti ratio on the evolution of precipitates and their effects on mechanical properties for $Ni_{35}(CoCrFe)_{55}AlxTi_{10-}x$ high entropy alloys. *J. Alloys Compd.* **2022**, *906*, 164291. [CrossRef]
29. Samal, S.; Rahul, M.R.; Kottada, R.S.; Phanikumar, G. Hot deformation behaviour and processing map of Co-Cu-Fe-Ni-Ti eutectic high entropy alloy. *Mater. Sci. Eng. A* **2016**, *664*, 227–235. [CrossRef]
30. Zhi, Q.; Tan, X.; Liu, Z.; Liu, Y.; Zhang, Q.; Chen, Y.; Li, M. Effect of Zr content on microstructure and mechanical properties of lightweight Al(2)NbTi(3)V(2)Zr(x) high entropy alloy. *Micron* **2021**, *144*, 103031. [CrossRef]
31. Li, R.; Gao, J.C.; Fan, K. Study to Microstructure and Mechanical Properties of Mg Containing High Entropy Alloys. *Mater. Sci. Forum* **2010**, *650*, 265–271. [CrossRef]
32. Jiang, S.; Lin, Z.; Xu, H.; Sun, Y. Studies on the microstructure and properties of AlxCoCrFeNiTi1-x high entropy alloys. *J. Alloys Compd.* **2018**, *741*, 826–833. [CrossRef]
33. Wang, Y.P.; Li, B.S.; Ren, M.X.; Yang, C.; Fu, H.Z. Microstructure and compressive properties of AlCrFeCoNi high entropy alloy. *Mater. Sci. Eng. A* **2008**, *491*, 154–158. [CrossRef]
34. Joseph, J.; Annasamy, M.; Kada, S.R.; Hodgson, P.D.; Barnett, M.R.; Fabijanic, D.M. Optimising the Al and Ti compositional window for the design of γ' (L12)-strengthened Al–Co–Cr–Fe–Ni–Ti high entropy alloys. *Mater. Sci. Eng. A* **2022**, *835*, 142620. [CrossRef]
35. Chen, Q.-s.; Lu, Y.-p.; Dong, Y.; Wang, T.-m.; Li, T.-j. Effect of minor B addition on microstructure and properties of AlCoCrFeNi multi-compenent alloy. *Trans. Nonferrous Met. Soc. China* **2015**, *25*, 2958–2964. [CrossRef]

Disclaimer/Publisher's Note: The statements, opinions and data contained in all publications are solely those of the individual author(s) and contributor(s) and not of MDPI and/or the editor(s). MDPI and/or the editor(s) disclaim responsibility for any injury to people or property resulting from any ideas, methods, instructions or products referred to in the content.